Jarvinen, Riku; Kallio, Esa

Energization of planetary pickup ions in the solar system

Published in:
Journal of Geophysical Research: Planets

DOI:
10.1002/2013JE004534

Published: 01/01/2014

Document Version
Publisher's PDF, also known as Version of record

Please cite the original version:
Jarvinen, R., & Kallio, E. (2014). Energization of planetary pickup ions in the solar system. *Journal of Geophysical Research: Planets*, *119*(119), 219236. https://doi.org/10.1002/2013JE004534

AGU PUBLICATIONS

JGR

Journal of Geophysical Research: Planets

RESEARCH ARTICLE

10.1002/2013JE004534

Key Points:
- Energization of atmospheric pickup ions varies considerably in the solar system
- Energization is weakest and most perpendicular to solar wind close to the Sun
- Energization is strongest during a declining phase of a solar cycle

Correspondence to:
R. Jarvinen,
riku.jarvinen@fmi.fi

Citation:
Jarvinen, R., and E. Kallio (2014), Energization of planetary pickup ions in the solar system, *J. Geophys. Res. Planets*, *119*, 219–236, doi:10.1002/2013JE004534.

Received 25 SEP 2013
Accepted 2 JAN 2014
Accepted article online 7 JAN 2014
Published online 28 JAN 2014

Energization of planetary pickup ions in the solar system

R. Jarvinen[1,2] and E. Kallio[1,3]

[1]Finnish Meteorological Institute, Helsinki, Finland, [2]Laboratory for Atmospheric and Space Physics, University of Colorado Boulder, Boulder, Colorado, USA, [3]School of Electrical Engineering, Aalto University, Helsinki, Finland

Abstract We study the solar wind-induced ion escape from planetary atmospheres at different radial heliospheric distances in the solar system. We derive histograms of the gyroaveraged $E \times B$ velocities, energies, and Larmor radii of planetary ions in the solar wind at Mercury, Venus, Earth, and Mars. The statistical analysis is based on the interplanetary Pioneer Venus Orbiter and OMNI solar wind data sets. In addition to the energization in the undisturbed solar wind we also model how planetary heavy ions get energized in the solar wind interaction of an unmagnetized planet at different distances to the Sun. We found that due to the Parker spiral, pickup ions are expected to be found on average at lower energies and at velocities more perpendicular to the solar wind flow, the closer to the Sun a planet or a comet is. According to a global hybrid simulation, planetary heavy ion energization is influenced qualitatively in a similar way in the presence of an induced magnetosphere than in the upstream solar wind under different Parker spiral angles due to fact that the structure of an induced magnetosphere depends strongly on the interplanetary magnetic field and solar wind conditions. Finally, the energization and dynamics of the pickup ions vary considerably with the solar activity. The variation is stronger the farther away from the Sun an object is. The Larmor radii of the pickup ions are largest during a solar minimum while the pickup ion energies are highest during the declining phase of a solar cycle.

1. Introduction

Our solar system has four terrestrial planets, which all differ from each other. Venus and Mars are planets without a global intrinsic magnetic field and they lose ions from their upper atmospheres due to the interaction with the solar wind [e.g., *Fedorov et al.*, 2011; *Barabash et al.*, 2007a]. The Earth is strongly magnetized and the solar wind does not directly interact with the terrestrial atmosphere. Mercury is the closest planet to the Sun in the solar system and it possesses also a global intrinsic magnetic field but it has only a tenuous exosphere.

It is not known how much heavy elements, such as oxygen, which is a typical upper atmospheric constituent at the terrestrial planets, the solar wind-induced ion escape has removed from the terrestrial planets nor how important the solar wind has been compared to other escape processes during the evolution of the solar system [e.g., *Lammer et al.*, 2008].

The magnetized solar wind provides a large-scale energy source to accelerate planetary ions at an unmagnetized planet, since a convection electric field is induced in the rest frame of the planet. As a result, planetary ions are energized and escape in the direction of the solar wind convection electric field [e.g., *Lundin*, 2011]. The fluxes and energies of planetary ions are larger on the hemisphere around an unmagnetized planet where the solar wind convection electric field is pointing away from the planet [e.g., *Luhmann et al.*, 2006; *Barabash et al.*, 2007a, 2007b]. The acceleration and escape of planetary ions in the solar wind are sometimes referred as the $E \times B$ pickup. In this study we call a pickup ion a planetary ion that is accelerated by the solar wind flow in the undisturbed solar wind or in the magnetosheath.

In addition to the $E \times B$ pickup there are also other solar wind-induced, nonthermal energization mechanisms of planetary ions. Downstream of planetary bow shocks smaller scale electric fields compared to the solar wind convection electric field and draped magnetic fields lead to energization of ions of atmospheric origin. Further, at low altitudes close to a planet densities of atmospheric neutral species are high and, thus, there is a larger source of planetary ions, which can affect plasma dynamics in an induced magnetosphere. The acceleration mechanisms of planetary ions are under active research based on observations and modeling. Different acceleration mechanism are discussed, for example, in *Lundin* [2011]. Although there exist several energization mechanisms, the $E \times B$ pickup is the underlying largest scale energy source for the acceleration of escaping planetary pickup ions.

The solar wind carries the Sun's magnetic field in the interplanetary space. When the solar wind expands in the heliosphere, the interplanetary magnetic field (IMF) is turned from almost radial configuration near the Sun to more perpendicular to the flow and in a spiral structure. This is called the Parker spiral [*Parker*, 1963]. According to *Slavin and Holzer* [1981], an average Parker spiral angle is ~20° at Mercury, 36° at Venus, 45° at Earth, and 57° at Mars. The angle between the solar wind velocity vector and the IMF vector is called the IMF cone angle. If the IMF vector is in the equatorial plane and the solar wind flow is radial, the spiral and cone angle are the same, which we assume in this work.

The Parker spiral is simple, average model of the IMF structure in the heliosphere and disturbances traveling from the Sun such as coronal mass ejections alter the solar wind and IMF properties in interplanetary space constantly. Further, the solar activity is associated with variations in the IMF and the solar wind conditions over a solar cycle [e.g., *Luhmann et al.*, 1993].

Distributions and dynamics of planetary O^+ ions in the plasma environments of Venus and Mars have been studied in several data analysis and test particle works. For example, see Venus studies by *Phillips et al.* [1987] and *Luhmann et al.* [2006] and Mars studies by *Luhmann and Schwingenschuh* [1990], *Cravens et al.* [2002], *Fang et al.* [2008], and *Nilsson et al.* [2012].

Further, many self-consistent simulation models have been applied to study different aspects of ion escape and plasma interactions at the terrestrial planets. Especially, the solar wind interactions of Venus and Mars have been studied by hybrid and MHD simulations [see, e.g., *Ledvina et al.*, 2008; *Brain et al.*, 2010, and references therein].

Luhmann [2003] analyzed the behavior of pickup ions in the heliosphere in a test particle study assuming the Parker spiral configuration of the IMF. In the study it was found that the evolution of pickup ions moving outward in the heliosphere carries information about their planetary or interstellar origin including location of ionization and initial velocity.

Even though the Parker spiral structure is a well-known feature of the IMF, the effect of the heliospheric distance of a planet from the Sun on the solar wind-induced planetary ion escape has not been studied much. Further, the importance of the Parker spiral angle has not been analyzed in comparative studies of planetary plasma interactions.

In this study we consider the energization of planetary ions by the solar wind at the terrestrial planets in the solar system. The work consists of two parts, which explore different spatial regions of planetary plasma environments. First, we derive detailed distributions of the pickup ion properties in the upstream solar wind at Mercury, Venus, Earth, and Mars over a solar cycle based on observations. We separate the motion of a pickup ion in the gyro (Larmor) motion and in the $E \times B$ guiding center drift. In homogeneous fields the drift motion is purely the $E \times B$ drift. The statistical analysis gives information about the part of planetary ion population that originates directly or are transported in the undisturbed solar wind. Second, we analyze the O^+ ion energization in the interaction between an unmagnetized planet and the solar wind in a self-consistent global hybrid simulation under different Parker spiral angle conditions of the IMF. The model includes all regions of an induced magnetosphere including the magnetosheath and the wake. Thus, the model analysis describes how an induced magnetosphere affects the energization of escaping planetary ions.

The study is organized as follows. In section 3 we derive analytical results for the $E \times B$ drift and for the pickup ion gyroaveraged speed and kinetic energy. Next we introduce the data sets (section 4) and the HYB hybrid simulation model (section 5) used in this study. Then in section 6 we determine the pickup ion properties in the undisturbed solar wind at the terrestrial planets based on in situ solar wind and IMF observations. In section 7 we present the simulation results of planetary ion energization in an induced magnetosphere under different Parker spiral angles. At the end we synthesize and discuss our findings.

2. Coordinate System

The coordinate system used in this study is defined as follows. The solar wind flow is assumed to be radial along the $-X$ axis: $\vec{U}_{SW} = (-U_{SW}, 0, 0)$. The $+Y$ axis is along the perpendicular IMF component to $\vec{U}_{SW}$: $\vec{B}_{SW} = (B_x, B_y, 0)$. Thus, the solar wind convection electric field is along the $+Z$ axis: $\vec{E}_{SW} = -\vec{U}_{SW} \times \vec{B}_{SW} = U_{SW} B_y \hat{e}_z$. The aberration caused by the planetary motion around the Sun is neglected. Radial distance to the Sun is denoted by r. Since the Y axis is set along the IMF perpendicular component and the solar wind is

assumed to flow along the $-X$ axis, we refer to the angle between the solar wind velocity and the IMF as the IMF spiral angle.

3. Equations: Guiding Center Motion and Gyroaverage

In this section we summarize the analytical formula for the $E \times B$ drift velocity in the solar wind and for the velocity and energy of a pickup ion averaged over a gyroperiod. A more complete treatment can be found, for example, in *Cloutier et al.* [1974]. See *Coates* [2004] and references therein for a more recent review of pickup ion dynamics. Further, analysis of pickup ions from planetary exospheres can be found in *Hartle et al.* [2011].

3.1. $E \times B$ Drift

The $E \times B$ drift velocity is defined as $\vec{V}_{E\times B} = \vec{E} \times \vec{B}/B^2$. Substituting $\vec{E} = \vec{E}_{\rm SW}$ and $\vec{B} = \vec{B}_{\rm SW}$ expressed in our coordinate system we get

$$\vec{V}_{E\times B} = U_{\rm SW}\left(\frac{B_x B_y}{B_x^2 + B_y^2}\hat{e}_y - \frac{B_y^2}{B_x^2 + B_y^2}\hat{e}_x\right) = \vec{U}_{\rm SW\perp}. \tag{1}$$

Thus, the guiding center of a pickup ion has a velocity vector in the XY plane. Equation (1) equals to the projection of $\vec{U}_{\rm SW}$ perpendicular to $\vec{B}_{\rm SW}$. The magnitude of the $E \times B$ drift reads

$$V_{E\times B} = U_{\rm SW}\sqrt{\frac{B_y^2}{B_x^2 + B_y^2}} = U_{\rm SW\perp}. \tag{2}$$

3.2. Gyromotion

The Larmor radius of a pickup ion starting at rest is

$$r_{\rm L} = \frac{mV_\perp}{qB} = \frac{mV_{E\times B}}{qB}, \tag{3}$$

where $V_\perp$ is the velocity perpendicular to $\vec{B}$ and m and q are the mass and charge of the particle.

A pickup ion starting at rest with respect to the solar wind forms a ring-shaped velocity distribution when it is accelerated and picked up in the flow [e.g., *Coates*, 2004, Figure 4]. The center of the ring in velocity space is at $\vec{V}_{E\times B}$. The velocity of a pickup ion can be written as a function of the gyrophase (α) as [e.g., *Cloutier et al.*, 1974]

$$v_{xy}(\alpha) = V_{E\times B}(1 - \cos\alpha) \tag{4}$$

$$v_z(\alpha) = V_{E\times B}\sin(\alpha), \tag{5}$$

where v_z is the velocity component parallel to $\vec{E}_{\rm SW}$ and v_{xy} is the velocity component perpendicular to $\vec{B}_{\rm SW}$ and to v_z. That is, v_{xy} is along $\vec{V}_{E\times B}$ (equation (1)).

Using a trigonometric identity the speed of a pickup ion comes as follows:

$$v(\alpha) = \sqrt{v_{xy}^2 + v_z^2} = \sqrt{2}V_{E\times B}\sqrt{1 - \cos(\alpha)}. \tag{6}$$

The speed of a pickup ion averaged over a gyroperiod is obtained by integration:

$$V_{\rm avg} = \frac{1}{2\pi}\int_0^{2\pi} {\rm d}\alpha\, v(\alpha) = \frac{4}{\pi}V_{E\times B} \approx 1.27V_{E\times B}. \tag{7}$$

Similarly, we get for the kinetic energy of a pickup ion averaged over a gyroperiod:

$$E_{\rm kin,avg} = \frac{1}{2\pi}\int_0^{2\pi} {\rm d}\alpha\left(\frac{1}{2}mv^2\right) = 2\times\left(\frac{1}{2}mV_{E\times B}^2\right). \tag{8}$$

That is, the gyroaveraged speed of a pickup ion is about 1.27 times $V_{E\times B}$ and the gyroaveraged kinetic energy of a pickup ion is 2 times the kinetic energy of a similar ion moving at $V_{E\times B}$. Further, the maximum speed of a pickup ion is 2 times $V_{E\times B}$ and the maximum kinetic energy of a pickup ion is 4 times the energy of a similar ion moving at $V_{E\times B}$. The speed and energy maxima occur at $\alpha = 180°$.

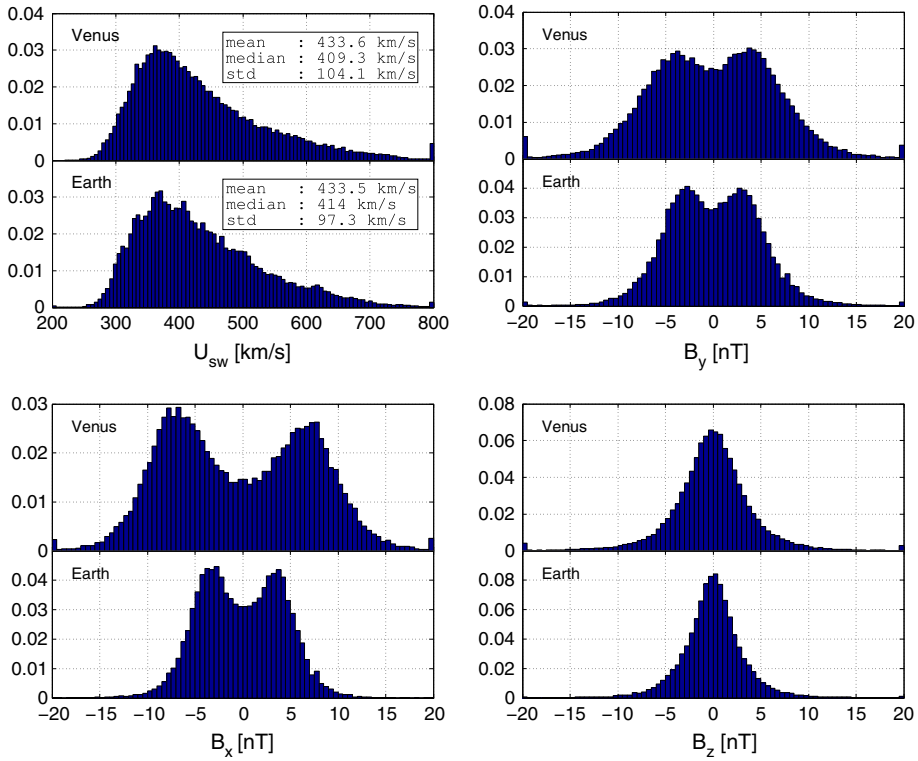

Figure 1. Histograms of the used solar wind and IMF data sets at Venus (PVO interplanetary data) and Earth (OMNI data). The shown components of the magnetic field are in the original coordinates of the used data sets. That is, the PVO magnetic data is in the VSO coordinates and the OMNI magnetic data is in the GSE coordinates. The vertical axis gives the number of samples in each bin divided by the total number of samples. Listed are also the mean, median, and standard deviation (std) values of the solar wind speed. Energies below and above the axes limits are shown in the first and last bin. See text for details.

4. Data Sets

We use two data sets to derive pickup ion properties at the terrestrial planets in the solar system. The Pioneer Venus Orbiter (PVO) 1 h averaged IMF and solar wind data [*Colin and Hunten*, 1977] from December 1978 to August 1988 are used to derive the pickup ion properties at Venus ($r = 0.723$ AU). The 1 h averaged OMNI solar wind and IMF data [*King and Papitashvili*, 2005] are used to derive the pickup ion properties at Earth ($r = 1.0$ AU) during the same time period.

We assume that U_{SW} given in the data sets is along $-X$ and we determine the IMF perpendicular component to the flow in our coordinate system as $B_y = \sqrt{B_y'^2 + B_z'^2}$, where B_y' and B_z' are in the Venus Solar Orbital (VSO) coordinates (PVO data) and in the Geocentric Solar Ecliptic (GSE) coordinates (OMNI data).

Further, we extrapolate the PVO interplanetary data to Mercury ($r = 0.387$ AU) and the OMNI data to Mars ($r = 1.524$ AU) by assuming the IMF scaling of $B_x \propto r^{-2}$ and $B_y \propto r^{-1}$ and a constant U_{SW} [e.g., *Slavin and Holzer*, 1981].

The data covers the maximum and declining phases of the Solar Cycle 21, the minimum between the Solar Cycles 21 and 22, and most of the rising phase of the Solar Cycle 22.

Figure 1 shows a comparison of U_{SW}, B_x, B_y' and B_z' histograms between the used PVO and OMNI data. The distribution of U_{SW} has a mean of about 430 km s^{-1} in both data sets and they display also other similar statistical characteristics. Thus, the results of the current analysis are not related to different U_{SW} in the two data sets. Further, the IMF components show similar sector structures in Figure 1 between the PVO and OMNI data sets except that the IMF is weaker at Earth than at Venus as expected.

The PVO interplanetary data has been used in a study by *Luhmann et al.* [1993] to compare the IMF and solar wind conditions and to analyze the solar cycle effects at Venus and at Earth. Further, we used in our earlier work the PVO interplanetary data to study the solar wind and IMF conditions and their correlations at Venus [*Jarvinen et al.*, 2008].

Table 1. Details and Upstream Conditions of the Five HYB-Venus Simulation Runs (Run 1–5) With Different Upstream IMF Spiral Angles Analyzed in This Work

Parameter	Value
Box size ($x \times y \times z$) [R_V]	$(-3...3) \times (-4...4) \times (-4...4)$
Grid cells ($n_x \times n_y \times n_z$)	$60 \times 80 \times 80$
Grid cell size (Δx^3)	$(0.1R_V)^3 \approx (605\ \text{km})^3$
Average macroparticles per cell	30
Time step (Δt)	40 ms
Solution snapshot time	400 s (20 s temporal average)
Obstacle radius	$R_V + 300$ km
Particle absorption radius	$R_V + 200$ km
IMF B_x (Run 1–5)	0, −1.0, −3.4, −7.0, and −16.2 nT
IMF [B_y, B_z]	[5.88, 0] nT
IMF spiral angle (Run 1–5)	90°, 80°, 60°, 40° and 20°
Convection electric field	[0, 0, 2.5] mV m^{-1}
Solar wind H^+ (V, n, T)	430 km s^{-1}, 14 cm^{-3}, 10^5 K
Electron temperature	10^4 K
Resistivity $\eta_a(r)$	Constant for $r > R_V + 300$ km, zero $r < R_V + 300$ km
H^+ photo ion production rate	6.42×10^{24} s^{-1}
H^+ ionospheric emission rate	5.0×10^{24} s^{-1}
O^+ photo ion production rate	4.09×10^{24} s^{-1}
O^+ ionospheric emission rate	1.0×10^{25} s^{-1}
Ionospheric emission radius	$R_V + 400$ km
Solar EUV photo rates	Solar minimum

5. Global HYB Hybrid Simulation

The global three-dimensional HYB hybrid simulation developed at the Finnish Meteorological Institute is used in this work to study how a planetary plasma environment affects the ion escape from an unmagnetized planet when the IMF spiral angle is changed. In the HYB hybrid simulation ions are modeled as macroparticle clouds in the Lorentz force field and electrons are a charge neutralizing fluid. The magnetic field is propagated by the Faraday's law. Advantage of a hybrid model is that there is no presumption of the ion velocity distributions and the ion dynamics are self-consistently coupled with the electric and magnetic field.

Venus is used as an example unmagnetized planet in the hybrid simulation runs analyzed here. In the HYB-Venus model planetary oxygen and hydrogen ions are created by photoionization of exospheric neutral coronae and by emission from the inner boundary (the ionospheric emission). The inner boundary mimics the exobase above a super conducting obstacle in the solar wind flow. See *Jarvinen et al.* [2009, and references therein] for details of the HYB-Venus model, which is used in this study.

5.1. Simulation Runs

Five HYB-Venus runs with stationary upstream conditions were performed for this study. The runs are identical except that the upstream IMF flow-aligned component (B_x) was changed between them. The B_x changes correspond to the change in the upstream IMF spiral angle between 90° and 20°. The 90° is the case when the upstream $\vec{B}_{SW}$ is perpendicular to $\vec{U}_{SW}$. Upstream conditions and numerical parameters of the runs are listed in Table 1.

The runs analyzed here are quite similar to the two high-resolution HYB-Venus runs used in *Jarvinen et al.* [2013] to study the hemispheric asymmetries of the Venus plasma environment except the current runs have a lower spatial resolution. The runs analyzed here are used specifically for the analysis of planetary O^+ ion energization in the Venusian plasma environment as a function of the IMF spiral angle. See *Jarvinen et al.* [2013] for more detailed description of the HYB-Venus runs and analysis of the Venusian plasma environment under different IMF spiral angle conditions.

In order to keep the analysis of simulation runs conclusive and quantitative we changed only one parameter, the flow-aligned component of the upstream IMF, between the runs. The differencies in ion energization between the runs are therefore due to the IMF spiral angle and they are not related, for example, to the solar wind convection electric field, which is the same in all the runs.

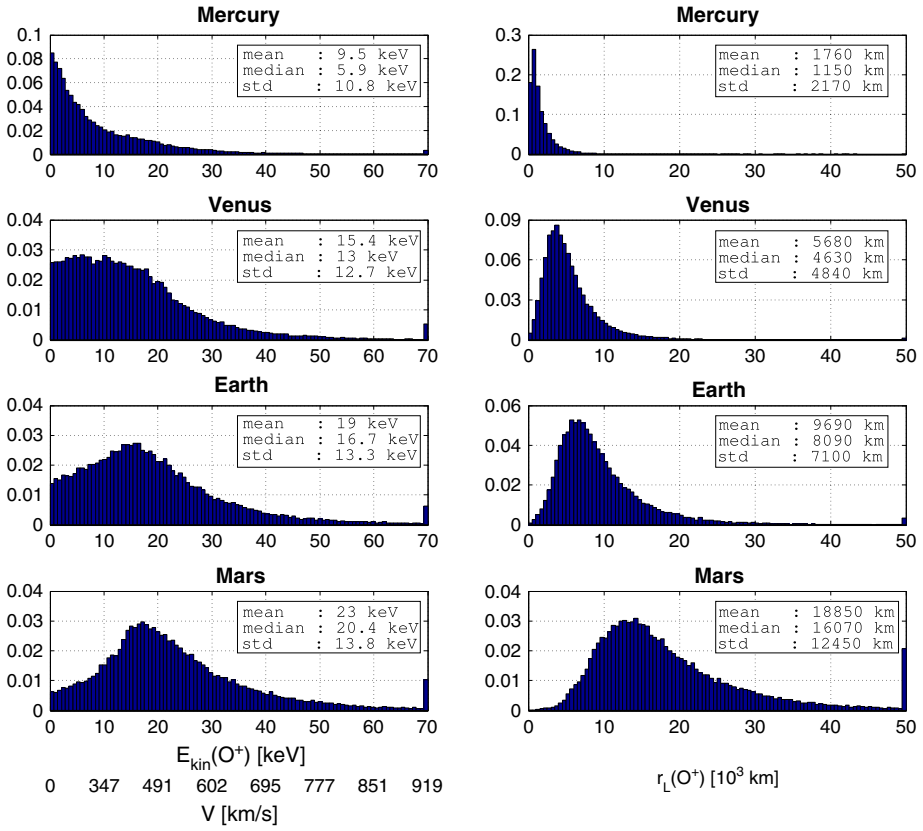

Figure 2. Histograms of the pickup O^+ gyroaveraged kinetic energies and Larmor radii in the solar wind at Mercury, Venus, Earth, and Mars. The vertical axis gives the number of samples in each bin divided by the total number of samples. Listed are also the mean, median and standard deviation (std) values of the histograms. Energies above 70 keV and radii above 50,000 km are shown in the last bin. See text for details.

6. Results: Observation Statistics

In this section we analyze the histograms of gyroaveraged kinetic energies and Larmor radii of O^+ pickup ions and the two-dimensional histograms of $\vec{V}_{E\times B}$ components in the solar wind at Mercury, Venus, Earth, and Mars using the data sets described in the previous section.

Figure 2 (left) displays the histograms of the gyroaveraged kinetic energies of an O^+ pickup ion calculated from equations (2) and (8). From the figure it can be seen that the closer to the Sun the planet is, more lower energies and less higher energies occur. At Mercury O^+, pickup energies of 1 keV or less are the most typical, and at Venus, the energies around 5–10 keV are the most typical. At Earth the most typical energy is about 15 keV and at Mars about 17 keV. At Venus there are roughly as many 1 keV and 10 keV pickup O^+ energies, whereas at Earth and at Mars, the occurrence of energies below the most frequent pickup energy decline.

Figure 2 (right) show the histograms of the Larmor radii of an O^+ pickup ion calculated from equations (2) and (3). It is evident that the Larmor radius increases with increasing distance to the Sun. The peak of the histogram is about at $r_L = 1000$ km, 4000 km, 6000 km, and 13,000 km at Mercury, Venus, Earth, and Mars, respectively. Further, at Earth and Mars the occurrence rate of Larmor radii above 20,000 km is nonzero, whereas at Venus and Mercury there are not many this kind of cases.

In Figure 3 the two-dimensional histograms (probability density maps) of the $\vec{V}_{E\times B}$ components determined by equation (1) are shown. Note that the coloring gives the occurrence probability of the $\vec{V}_{E\times B}$ components in each bin divided by the total number of samples, and the figure does not represent the pickup ion velocity distribution.

From Figure 3 it can be seen that the most frequent (red) areas are more concentrated on the $|V_{E\times B,x}| < |V_{E\times B,y}|$ cases, that is, the $E \times B$ drift is directed usually more perpendicular to $\vec{U}_{SW}$ than along $\vec{U}_{SW}$ the closer to the Sun the planet is. At Mercury and at Venus most cases are like this. At Earth and at Mars there

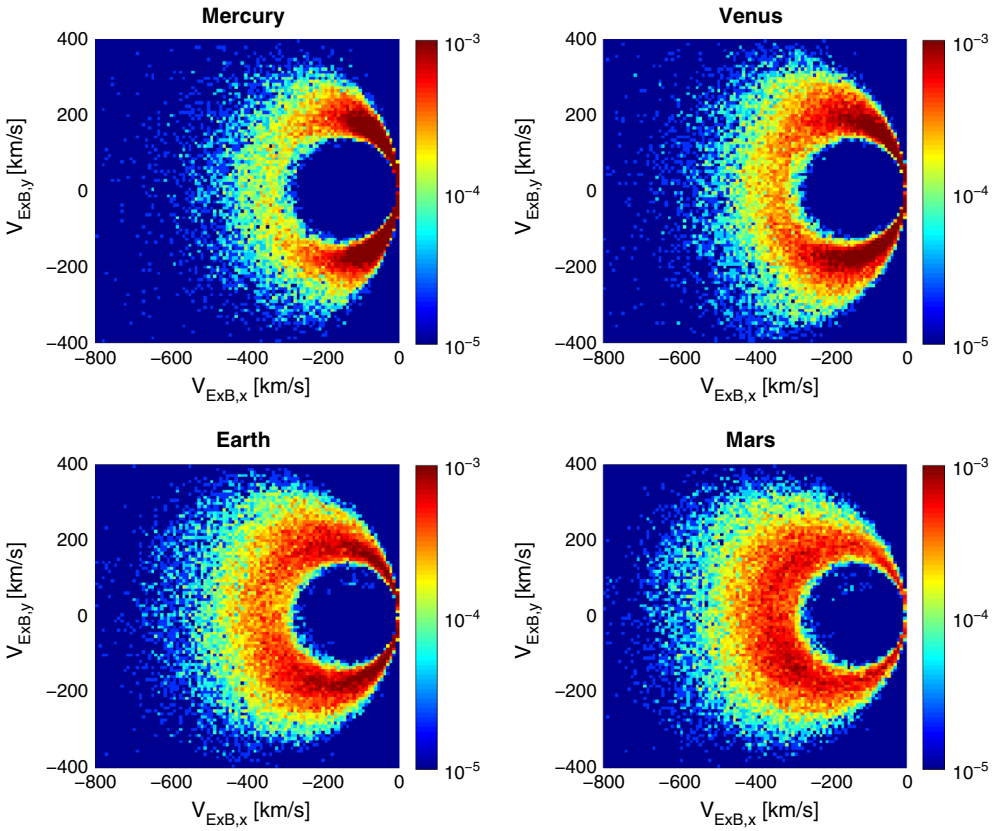

Figure 3. Two-dimensional histograms (probability density maps) of the $E \times B$ drift velocity components in the solar wind at Mercury, Venus, Earth, and Mars. Note that the coloring gives the occurrence probability of the $E \times B$ drift velocity components in each bin divided by the total number of samples, and the figure does not represent the pickup ion velocity distribution. See text for details.

occurs roughly as many cases with $|V_{E\times B,x}| > |V_{E\times B,y}|$ as there are cases with $|V_{E\times B,x}| < |V_{E\times B,y}|$. But, the occurrences get scattered spherically around the histogram when moving away from the Sun.

There are almost no cases that have $|V_{E\times B,x}| < 250$ km s^{-1} and $|V_{E\times B,y}| < 100$ km s^{-1} in Figure 3, which is seen as a circle-shaped blue region in the middle right-hand side in all four panels. This is due to the fact that the occurrence of $U_{SW} \lesssim 250$ km s^{-1} is rare. Since $\vec{U}_{SW}$ is along $-X$ in the used coordinates, $V_{E\times B} < 250$ km s^{-1} values in Figure 3 are due to the projection of $\vec{U}_{SW}$ perpendicular to $\vec{B}_{SW}$ (equation (1)).

7. Results: Hybrid Simulations

In this section we present results from the HYB hybrid simulation model and analyze the effect of an induced magnetosphere and a planetary plasma environment in the solar wind-induced energization on planetary ions with different upstream IMF spiral angles. We use Venus as an example unmagnetized planet in the simulation. Four of the five performed runs for this study are visualized in Figures 4–6. In the visualized runs the IMF spiral angle is 90° (perpendicular case), 60°, 40°, and 20°.

Figure 4 shows the magnetic field in the simulation. When the spiral angle is small compared to the perpendicular (90°) case, a strong dawn-dusk asymmetry and a parallel bow shock and foreshock region arise as seen in Figures 4h–4i and 4k–4l. See more detailed analysis of the magnetic morphology of the Venusian induced magnetosphere under different IMF spiral angles in *Jarvinen et al.* [2013].

The effect of the IMF spiral angle on the solar wind-induced planetary O^+ ion escape is analyzed in Figures 5–7.

In the perpendicular case the O^+ ions move mostly along the solar wind electric field and the solar wind velocity (upper half of Figures 5a and 6a). The O^+ speed is higher the farther away from the planet along $\vec{E}_{SW}$ the ions are (magenta color in Figure 6), which is a result of the $E \times B$ pickup.

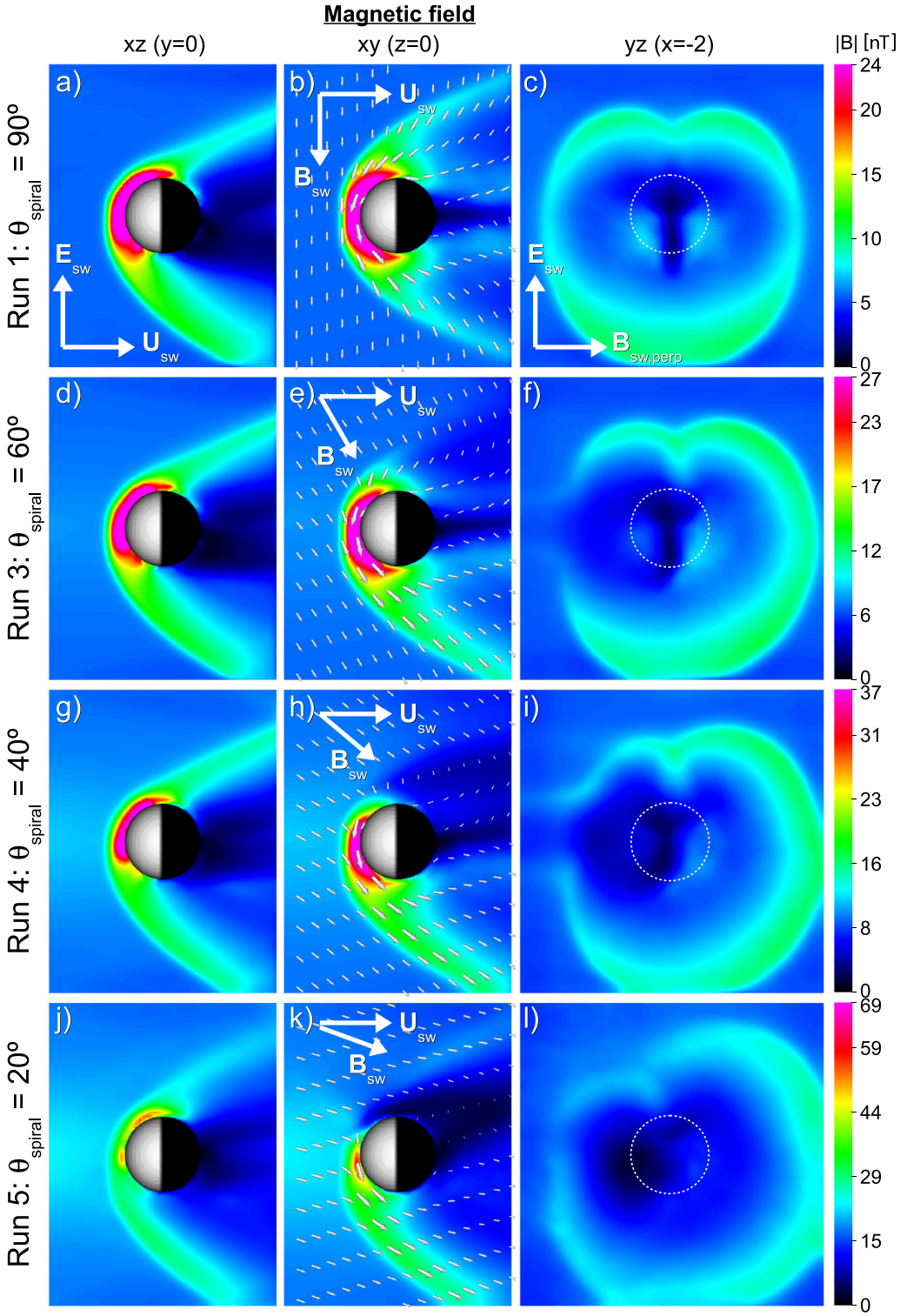

Figure 4. Magnetic field in the Venusian induced magnetosphere in four different Parker spiral angle cases in the global HYB-Venus hybrid simulation. (a–l) The 90° run (perpendicular), the 60° run, the 40° run, and the 20° run. Figures 4a, 4d, 4g, and 4j are the *XZ* ($Y = 0$) plane, Figures 4b, 4e, 4h, and 4k are the *XY* ($Z = 0$) plane, and Figures 4c, 4f, 4i, and 4l are the *YZ* ($X = -2R_v$) plane. The shown parameters are temporally averaged over 20 s to reduce the particle noise in the simulation. The small arrows on top of the color maps are the magnetic field vectors on the corresponding planes. To clarify the illustration maximum displayed vector size is 2 times the magnitude of the upstream IMF and the maximum of the color scale is 4 times the magnitude of the upstream IMF. The big arrows in Figures 4a–4c, 4e, 4h, and 4k give the orientation of the solar wind electric field ($\vec{E}_{sw}$), velocity ($\vec{U}_{sw}$), and the IMF ($\vec{B}_{sw}$). The sphere and the dashed circle have the radius of Venus and the gray hemisphere of the sphere is the dayside and the black hemisphere is the nightside of the planet.

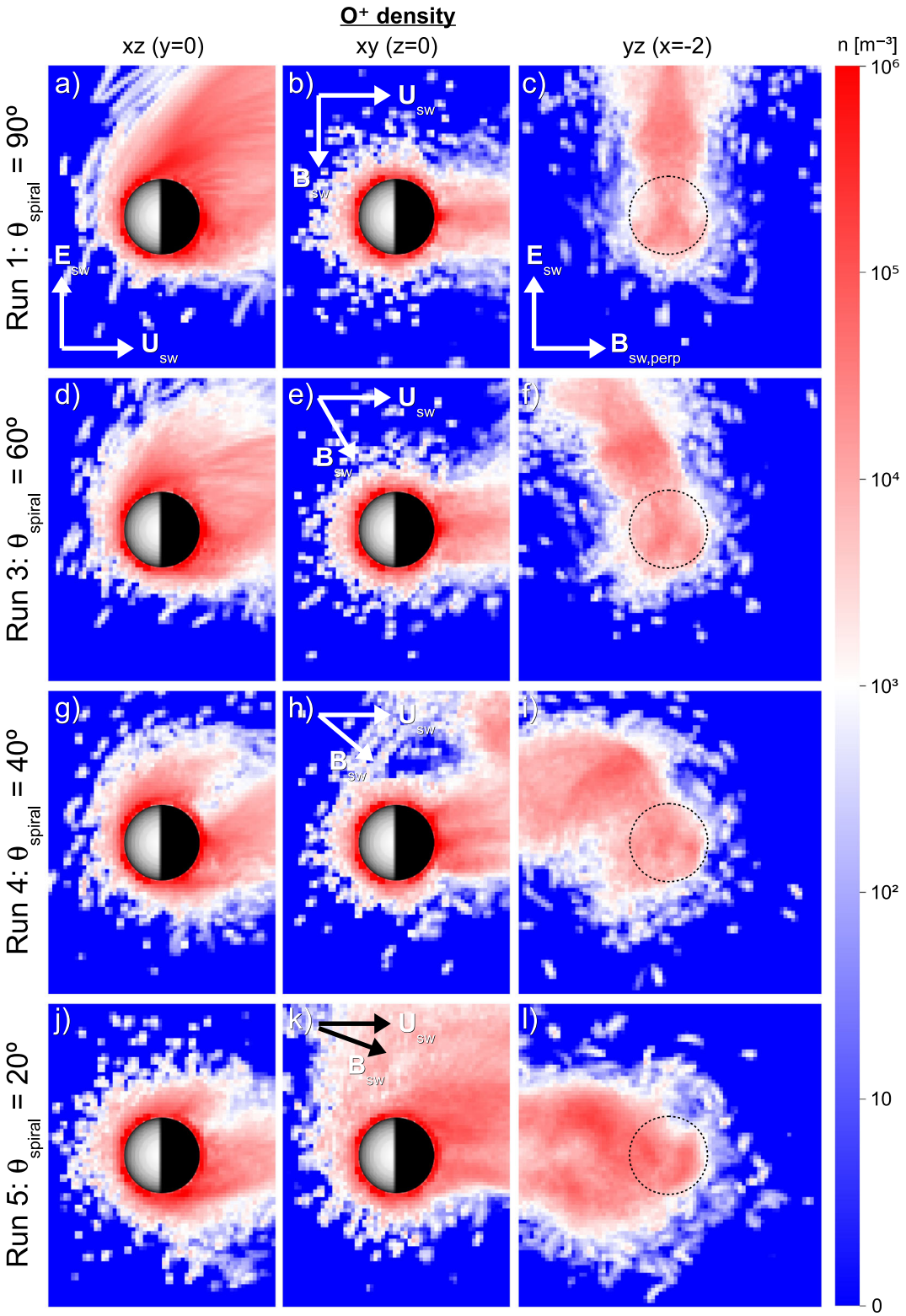

Figure 5. O^+ density in the Venusian induced magnetosphere in four different Parker spiral angle cases in the global HYB-Venus hybrid simulation. The figure is in the same format as Figure 4 except that the color scale is the same for all rows.

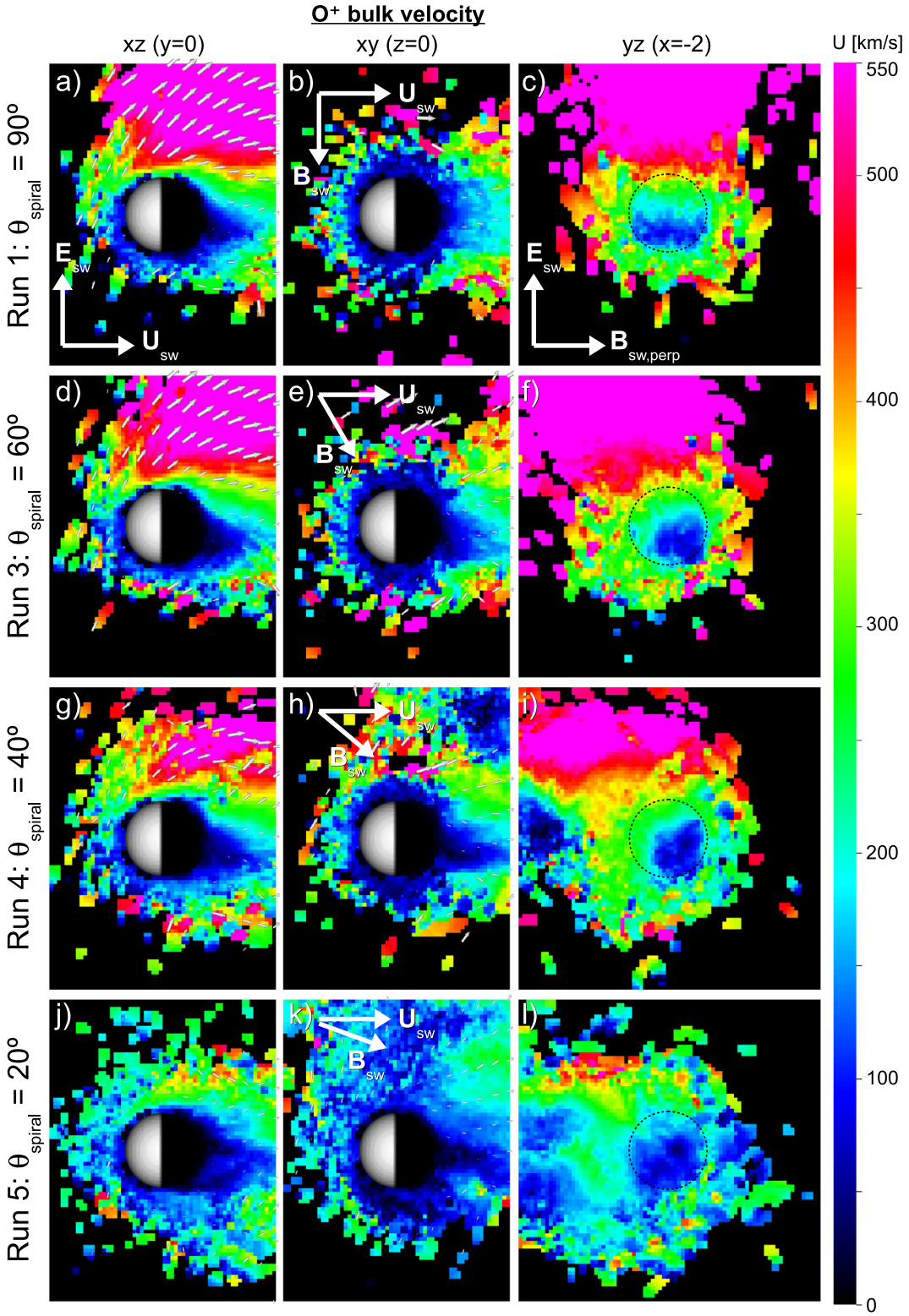

Figure 6. O^+ bulk velocity in the Venusian induced magnetosphere in four different Parker spiral angle cases in the global HYB-Venus hybrid simulation. The figure is in the same format as Figure 4 except that the color scale is the same for all rows and the displayed vectors are the O^+ velocity vectors with a maximum length of 550 km s^{-1}.

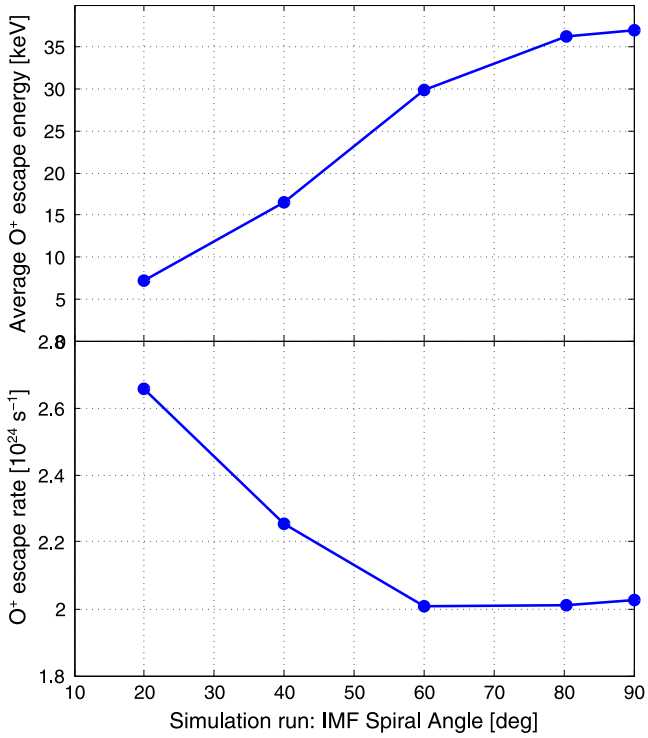

Figure 7. (top) Average energy per escaping O^+ ion and (bottom) total oxygen ion escape rate from Venus in five different Parker spiral angle cases in the global HYB-Venus hybrid simulation. The average energy is calculated as the total kinetic energy flux of O^+ ions escaping from the simulation box divided by the total O^+ escape rate from the simulation box.

However, when the IMF spiral angle decreases, the maximum O^+ speeds reduce as seen in Figure 6. Also, the escaping O^+ flow is always ~perpendicular to $\vec{B}_{SW}$, and thus, it is turned toward the hemisphere of the parallel bow shock resulting in a strong oxygen ion dawn-dusk asymmetry and more perpendicular O^+ bulk velocity to $\vec{U}_{SW}$ (see more detailed discussion in *Jarvinen et al.* [2013]).

In the IMF spiral angle case of 20° there is no magenta color at all and only little red in the O^+ velocity plot in Figures 6j–6l indicating that the speed of the escaping O^+ reach is only around 300 km s^{-1} or below within the simulation box. In the perpendicular run the O^+ ions reach locally 550 km s^{-1} and above speeds (Figures 6a–6c).

Figure 7 shows the average escape energy and escape rate of planetary O^+ ions from the simulation box in the analyzed HYB-Venus runs as a function of the IMF spiral angle. The escape rate is somewhat higher with spiral angles <60° compared to the spiral angle cases >60° (see more detailed discussion in *Liu et al.* [2009]). The average kinetic energy of escaping O^+ ions decreases in concert with decreasing spiral angle as seen in Figure 7 (top).

8. Discussion

The energization and dynamics of escaping planetary pickup ions in the undisturbed solar wind depend on $\vec{U}_{SW}$ and $\vec{B}_{SW}$ (equations (1) and (3)). Since these parameters depend on the distance from the Sun, the properties of pickup ions vary within the solar system. As shown in Figures 2 and 3, the lowest pickup ion energies and the most perpendicular pickup ion velocities to $\vec{U}_{SW}$ are expected close to the Sun and higher energies directed mostly along $\vec{U}_{SW}$ are expected at planets farther away from the Sun. Further, not only the average properties but also the distributions of the pickup ion properties are different at different distances to the Sun.

However, only part of the planetary ions are picked up directly in the undisturbed solar wind at unmagnetized planets. Most of the planetary ions originate inside an induced magnetosphere downstream of the bow shock and are energized in the planetary wake or in the magnetosheath. In addition to the analysis of

the $E \times B$ pickup in the undisturbed solar wind, we performed global hybrid simulations to study how the IMF spiral angle affects the energization of planetary heavy ions in an induced magnetosphere.

The morphology of the Venusian induced magnetosphere is strongly affected by the Parker spiral angle as seen in Figure 4. Further, the escape and energization of the planetary O^+ ions is also affected by these morphological changes (Figures 5–6). According to a hybrid simulation, the escaping planetary ions are found at lower energies and at velocities more perpendicular to the planet-Sun line when the IMF is more aligned with the solar wind velocity compared to the perpendicular case. Figure 7 (top) shows that an average oxygen ion escape energy from the simulation box is reduced in concert with the decreasing upstream spiral angle.

That is, the changes in ion escape energies and escape velocities as a function of distance from the Sun occur not only in the undisturbed solar wind (section 6) but also in a global hybrid simulation of a plasma interaction of an unmagnetized planet (section 7). This is not completely unexpected because an induced magnetosphere and, especially, the magnetosheath of an unmagnetized planet are strongly controlled by the IMF and the solar wind.

8.1. IMF Spiral Angle

According to equation (2), the $E \times B$ velocity equals to the solar wind velocity if the IMF spiral angle is 90° (i.e., the IMF has only the perpendicular component). In the case of spiral angle other than 90°, the nonzero IMF B_x results in $V_{E \times B} < U_{SW}$ in equation (2). If we keep $\vec{E}_{SW}$ and $\vec{U}_{SW}$ constant (as was done in the simulation runs analyzed here), the changes in the IMF spiral angle correspond to the changes in the IMF B_x. Further, this results in changes in the $E \times B$ velocity.

Adding a nonzero B_x to the magnetic field (while keeping B_y fixed) increases the $\vec{B}$ magnitude and, thus, decreases the Larmor radius of a pickup ion (equation (3)). The smaller Larmor radius means that a pickup ion starting at rest moves along $\vec{E}_{SW}$ a shorter distance before it is turned against $\vec{E}_{SW}$ at gyrophase $\alpha = 180°$ compared to the $B_x = 0$ case. The smaller distance along the same convection electric field means less electric potential difference and, thus, less kinetic energy for the pickup ion according to the energy principle.

Another way to describe the dependence of the pickup ion energy on the spiral angle is the projection of $\vec{U}_{SW}$ along $\vec{V}_{E \times B}$. The magnitude of the $E \times B$ velocity equals to the magnitude of the solar wind velocity vector projected along $E \times B$ direction. When the IMF is perpendicular to the solar wind flow, the $E \times B$ drift velocity is the same as the solar wind velocity. However, when the IMF has a flow-aligned component, the $E \times B$ drift has a component perpendicular to the solar wind velocity (equation (1)). Thus, the projection reduces the magnitude of the $E \times B$ velocity.

When the solar wind $\vec{U}_{SW}$ and the IMF B_y are kept constant and B_x is let to increase without a limit, the $E \times B$ velocity approaches asymptotically completely perpendicular orientation to $\vec{U}_{SW}$ and zero magnitude.

Note that the discussion here is concentrated on the effect of the IMF spiral angle. In practice, as seen in section 4, solar wind parameters have temporal variations and both the IMF spiral angle and the solar wind convection electric field can change in the same time. In this case the changes in the pickup ion energization (the changes in the electric potential difference) depend not only on the spiral angle and the Larmor radius of a pickup ion but also on the solar wind convection electric field.

The IMF spiral angle affects the energization of planetary ions also downstream of a bow shock as seen in the global Venus hybrid simulation analyzed here in Figures 4–7 (see more detailed discussion in *Jarvinen et al.* [2013]). Moreover, the spiral angle has an effect on the global O^+ escape rate (see more detailed discussion in *Liu et al.* [2009]). These changes occur even though the solar wind convection electric field is the same in all runs.

The difference in the global O^+ escape rate in the simulation runs (Figure 7, bottom) is about 25% between the perpendicular run and the 20° Parker angle run. The average energy per escaping O^+ ion in the perpendicular case is about 5 times the energy in the 20° Parker angle run.

In the model there are not many planetary O^+ ions originating directly in the upstream solar wind as neutral corona densities at those altitudes are low. However, many O^+ ions get in the upstream solar wind and the magnetosheath due to their gyroradii and then undergo the $E \times B$ pickup. This is why the average kinetic

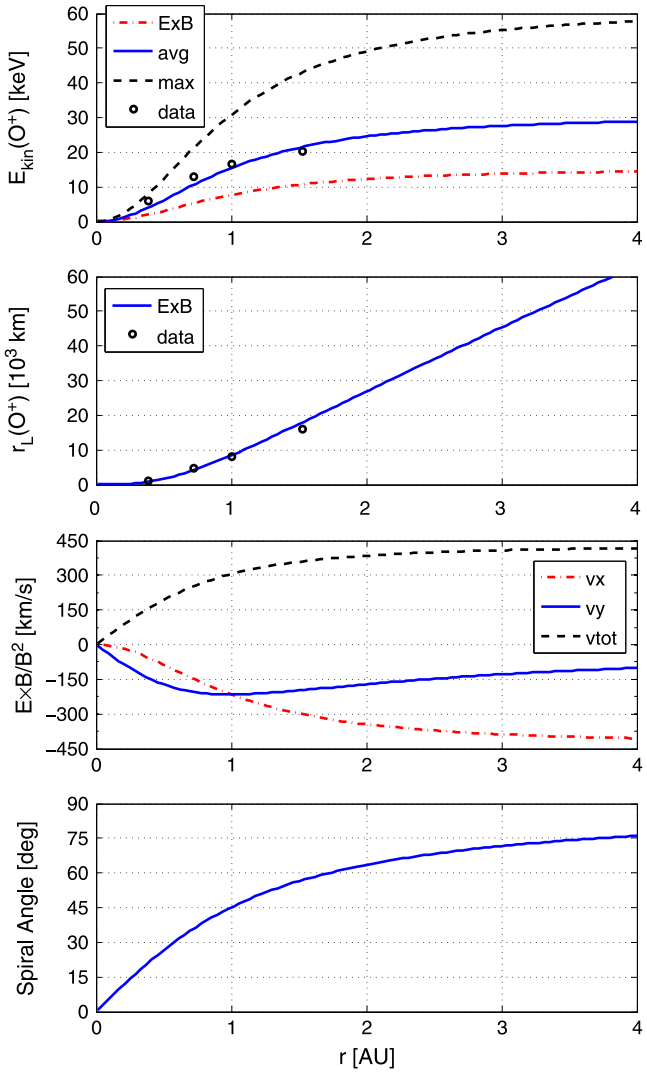

Figure 8. (first panel) Pickup O^+ kinetic energy and (second panel) Larmor radius, (third panel) the $E \times B$ drift velocity and (fourth panel) the IMF spiral (or cone) angle as a function of radial distance from the Sun based on the Parker spiral configuration of the IMF. Three different kinetic energies are shown: the $E \times B$ energy (equation (2)), the gyroaveraged energy (equation (7)), and the maximum energy over a gyroperiod. Dots show the median values of E_{kin} and r_L from Figure 2. See text for details.

energies of the escaping O^+ ions in the model change with the IMF spiral angle in the same way as in the upstream solar wind (Figure 7 (top) versus Figure 8 (first panel)).

8.2. Parker Spiral Model

To illustrate the above considerations of the IMF spiral angle we study the O^+ pickup ion properties in the Parker spiral model of the IMF with a constant solar wind velocity in Figure 8. The figure was plotted assuming the IMF spiral angle of 36° and 10 nT magnitude at Venus and a constant U_{SW} of 430 km s^{-1}. The normalization equals to $\vec{B}_{SW} = (-8.09, 5.88, 0)$ nT at Venus. The IMF was extrapolated from $r = 0$ to 4 AU by assuming the following scalings: $B_x \propto r^{-2}$ and $B_y \propto r^{-1}$.

The decline of the pickup ion energy and Larmor radius when moving toward the Sun is evident in the figure. Further, the v_y component of $\vec{V}_{E \times B}$ is a dominating component of the drift velocity at $r < 1$ AU. The v_x and v_y components of $\vec{V}_{E \times B}$ are equal at $r \approx 1$ AU, which equals to the 45° spiral angle.

An O^+ ion picked up in the 430 km s^{-1} solar wind flow with $B_x = 0$ has a gyroaveraged kinetic energy of ~31 keV (equations (2) and (8)). This "full" O^+ pickup energy is reached asymptotically only at distance of several AUs from the Sun in Figure 8. In the inner solar system ($r \lesssim 1.5$ AU), the nonzero B_x related to the

Parker spiral limits the occurrence of full pickup ion energies. The dots in Figure 8 show the median E_{kin} and r_L values of histograms in Figure 2.

8.3. Non-Parker Features

Even though the Parker model is consistent with the changes in average planetary pickup ion properties as a function of a distance to the Sun, it does not directly explain the shapes of histograms of the pickup ion properties in Figures 2–3. The exact shapes of the histograms are affected by the correlation of the IMF components and the solar wind velocity. These correlations can vary at different phases of a solar cycle and at different planets as the solar wind and solar disturbances expand from the Sun in the heliosphere. See the effect of space weather on planetary plasma environments and ion escape, for example, in *Futaana et al.* [2008], *Luhmann et al.* [2008], *McEnulty et al.* [2010], *Edberg et al.* [2011], and *Wei et al.* [2012].

8.4. Finite Larmor Radius Effects

The finite Larmor radius (FLR) effects of pickup ions are expected to be the strongest of the analyzed planets in the plasma environment of Mars, since the largest O^+ Larmor radii are found there (Figures 2 and 8) and, also, Mars has only ~half the radius of Venus or the Earth. The ratio of the median pickup O^+ Larmor radius and the radius of a planet at Mars is about six times the value at Venus. The FLR effects of escaping planetary heavy ions from Venus and Mars can be seen, for example, in *Nordström et al.* [2013, Figure 7] and in *Nilsson et al.* [2012, Figure 2].

Note that charged particle drifts, or the guiding center approximation, give accurate description of the motion of magnetized particles only. The detailed three-dimensional structure of the O^+ flow in the Venusian induced magnetosphere analyzed in Figures 5–6 cannot be explained by drift motions. Heavy ions such as O^+ are typically nonmagnetized due to their large gyroradii compared with the size of the interaction region whereas lighter species like H^+ follow the $E \times B$ drift [*Jarvinen et al.*, 2010]. However, in homogeneous fields the $E \times B$ velocity gives the gyroaveraged energy of pickup ions (equations (2) and (8)).

The O^+ flow turns from the *xz* plane in Run 1 toward the hemisphere of the parallel bow shock in Runs 3–4 and 5 when the IMF spiral angle is decreasing (Figures 5–6). Also the motion of the O^+ guiding centers approximated by the $E \times B$ drift in the undisturbed solar wind turns the same way. Even though the FLR effects are important for the dynamics of the escaping O^+ ions, the solar wind convection electric field is the underlying large-scale energy source also for these ions.

8.5. Solar Cycle Dependence

The occurrence rate of the solar wind and IMF conditions differ between the phases of the solar activity cycle, and different solar cycles can have different conditions [e.g., *Luhmann et al.*, 1993]. Thus, the connection between the solar activity and the interplanetary conditions means different $E \times B$ pickup properties.

Figure 9 displays yearly means and medians of the O^+ pickup ion kinetic energies and Larmor radii between 1979 and 1988 based on the same data set as Figures 2–3. (The year 1978 is not shown because there is less than a month of PVO interplanetary data from that year). Whereas Figures 2–3 give distributions of the whole data set, Figure 9 gives the variation of pickup ion properties as a function of solar activity.

Energization of the pickup ions in the solar wind is found to increase and peak during the decline of the Solar Cycle 21 in 1980–1984. On the other hand, Larmor radii of the pickup ions in the solar wind are largest during the solar minimum in 1985–1987.

The annual average of the solar wind velocity increased from 1980 until about 1984 [see *Luhmann et al.*, 1993, Figure 6] during the declining solar activity. Consequently, the pickup ion energies increased in the same time. Moreover, the annual average of the IMF magnitude decreased from 1983 until about 1987 [see *Luhmann et al.*, 1993, Figure 4] during the solar activity minimum leading to the increase of the pickup ion Larmor radii.

The changes in E_{kin} and r_L over a solar cycle are stronger in absolute magnitude the farther away from the Sun the planet is. Thus, the variation of pickup ion properties is strongest at Mars and weakest at Mercury of the planets analyzed here.

Further, the OMNI data over several solar cycles between 1963 and 2013 shows similar periodicities in the derived O^+ kinetic energy and Larmor radii at $r = 1$ AU as a function of solar activity as the data analyzed and shown here (figure not shown). That is, the pickup ion energization peaks during the decline of the solar

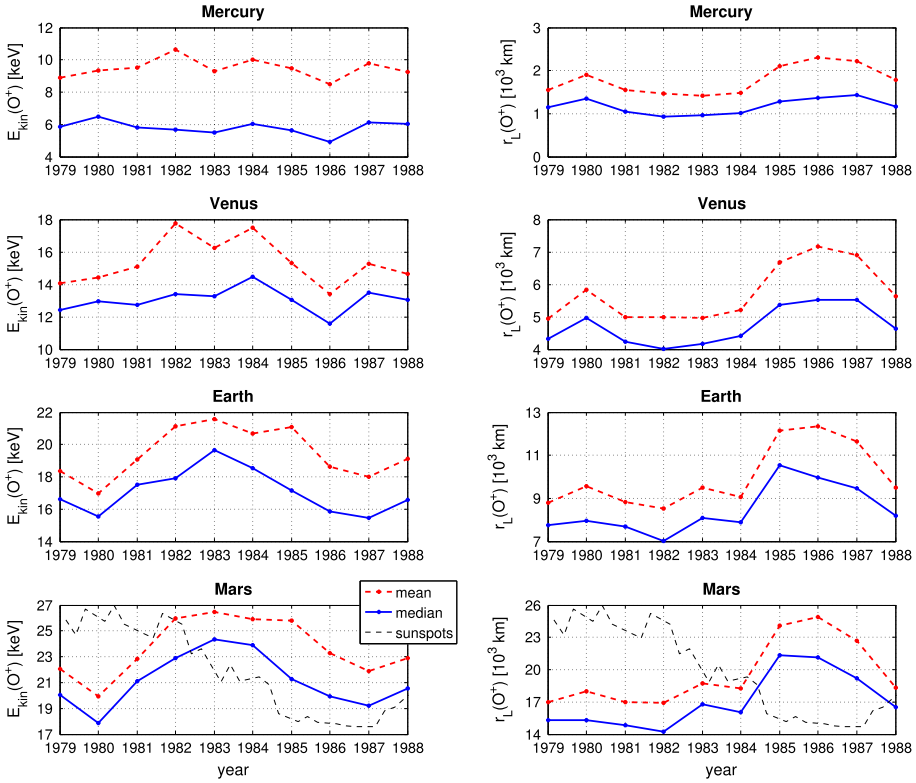

Figure 9. Yearly mean and median values of (left) the pickup O^+ gyroaveraged kinetic energies and (right) Larmor radii in the solar wind at Mercury, Venus, Earth, and Mars. (bottom) A 3 month average sunspot number from the OMNI data to illustrate the progress of the solar activity is shown. The unit of the sunspot number is arbitrary. See text for details.

activity and the Larmor radii peaks during the solar minima. Interestingly, during the declining phase and the deep minimum of the most recent solar cycle (Solar Cycle 24), the pickup ion energization was lower and the Larmor radii higher than compared to the previous Solar Cycles 19–23.

The yearly analysis shows that the ion pickup varies considerably with solar activity within a solar cycle and from cycle to cycle.

8.6. Induced Magnetosphere

According to global hybrid simulations analyzed here the IMF spiral angle affects the solar wind-induced heavy ion escape qualitatively in a similar way when a planetary plasma environment is present than in the undisturbed solar wind (compare Figures 7 (top) and 8 (first panel)). That is, the smaller the spiral angle, the smaller the escape energy and more perpendicular the escape velocity to the solar wind flow. This happens since many O^+ ions originating in an induced magnetosphere get in upstream the solar wind or in the magnetosheath due to their large gyroradii.

In this study we considered only the change in the IMF spiral angle in a global hybrid simulation. In reality also the solar wind density and temperature change as a function of the radial distance from the Sun. Moreover, the sizes of the terrestrial planets and, thus, the sizes of their plasma environments differ from each other (see, e.g., a comparison of Venus and Mars in *Fedorov et al.* [2008]). These parameters are not considered in this work but they can affect the energization of planetary ions. Detailed simulations and analysis of in situ observations are needed in the future to quantify the effect of all solar wind parameters (both stationary and nonstationary situations) to the ion escape at different planets.

Further, while the $E \times B$ velocity decreases with decreasing IMF spiral angle, the small spiral angle also gives rise to the parallel bow shock and foreshock regions in a planetary plasma environment (see Figures 4b, 4e, 4h, and 4k). The wave activity related to the turbulent parallel bow shock can lead to changes in the energization and escape of planetary ions [*Luhmann et al.*, 1987]. The statistical acceleration of planetary ions by plasma waves in small IMF spiral angle cases should be analyzed in a detailed study to determine its importance compared to the large scale $E \times B$ pickup.

8.7. Pickup Ion Species

Note that the analysis is not restricted to O^+ ions but the kinetic energies and Larmor radii in Figures 2, 8, and 9 can be scaled to any pickup ion species by multiplying the E_{kin} and r_L values by a factor of m_X/m_O, where m_X is the mass of the new species and m_O the oxygen mass. For example, the factor is ~1/16 for protons and 2 for O_2^+. In Figure 2 (left, bottom) also particle speeds are shown, which do not depend on the species. Also, the $E \times B$ drift velocity in Figures 3 and 8 is independent of particle species.

8.8. Exoplanets, Comets, and Mass Loading

Close-in exoplanets orbiting close to their star may experience stellar wind interactions where the incident plasma flow and the magnetic field are almost aligned [e.g., *Zhang et al.*, 2009; *Johansson et al.*, 2011]. The $E \times B$ pickup is not expected to be efficient in this kind of interaction due to the small IMF spiral angle.

Moreover, objects orbiting the Sun in highly noncircular orbits, such as comets, undergo changing conditions in ion pickup during their journey [e.g., *Coates*, 1997, 2004, and references therein]. Interestingly, comets become active when they are near the Sun, and in the same time, the energy of the pickup ions is expected to decrease due to the decreasing IMF spiral angle compared to the aphelion. That is, when a comet is active and producing a lot of ions near the Sun, the small spiral angle limits the $E \times B$ drift velocity.

Further, the mass loading of planetary or cometary ions in the solar wind is affected by the energy and momentum density in the solar wind, which decrease as $\propto r^{-2}$. When a fixed amount of newly born ions are created in the solar wind, their mass-loading effect depends how much there are energy and momentum in the flow.

But, also the IMF Parker spiral angle affects the mass loading. Introducing a new ion in the solar wind when the spiral angle is small has less mass-loading effect than in the case when the spiral angle is close to 90° if the solar wind velocity is the same. This is because in the more flow-aligned IMF case the $E \times B$ velocity is smaller (equation (2)), and, thus, a pickup ion need less energy and momentum from the flow to reach the $E \times B$ velocity, than in the perpendicular case. Further, when there is on average higher $E \times B$ velocity at large r due to the IMF spiral angle approaching 90°, the energy and momentum density of the solar wind are small.

The situation is more complicated when the number of new ions introduced in the solar wind is large (e.g., at comets) because more energy is needed from the flow to accelerate many ions compared to the one new ion case. When the energy and momentum needed for the pickup ion energization is of the same order of magnitude than the flow energy and momentum density, the mass loading decreases the solar wind speed and affects the plasma dynamics and the pickup ion energization. See, for example, *Kallio and Jarvinen* [2012, Figure 3] for the mass-loading effect in the HYB simulation.

At close distance to the Sun the pickup ion escape from celestial bodies may be limited by the small $E \times B$ velocity due to the small IMF spiral angle, while at larger distances the escape may become limited by the available ionization source and the energy and momentum density in the solar wind. The interplay between the IMF spiral angle, the source of pickup ions and the source of energy and momentum in the solar wind lead to a race against each other at different heliospheric distances.

9. Summary

We estimated the properties of the solar wind-induced planetary ion escape at the terrestrial planets in the solar system. We derived detailed histograms of velocities, energies, and Larmor radii of pickup ions in the solar wind at Mercury, Venus, Earth, and Mars based on the interplanetary PVO and OMNI data sets. We also studied the effect of an induced magnetosphere in the energies and dynamics of escaping planetary ions as a function of the angle between the solar wind velocity and the IMF, which is smaller the closer to the Sun a planet is. Further, we interpreted the average kinetic energies and Larmor radii of the pickup ions in terms of the Parker spiral model and analyzed the solar cycle dependence of the pickup ion properties.

We found in the data analysis that the pickup ions are expected to be found on average at lower energies and at smaller Larmor radii closer to the Sun an object, for example, a planet or a comet, is. The closer to the Sun, the more perpendicular to the solar wind flow the pickup ion velocity is on average. The decreased average energies and perpendicular velocities of the pickup ions close to the Sun are associated with the decreasing angle between the solar wind velocity and the IMF.

According to global hybrid simulations analyzed in this work planetary heavy ion energization is influenced in a similar way in the presence of an induced magnetosphere than in the upstream solar wind under different Parker spiral angles. This is due to the fact that the structure of an induced magnetosphere depends strongly on the IMF and solar wind conditions.

Finally, the energization and dynamics of the planetary pickup ions vary considerably with the solar activity. The variation is stronger the farther away from the Sun an object is. The Larmor radii of the pickup ions are largest during a solar minimum while the pickup ion energies are highest during the declining phase of a solar cycle.

Acknowledgments

The work of the lead author was supported by the Academy of Finland and the Magnus Ehrnrooth foundation. The PVO interplanetary data were obtained from NASA's National Space Science Data Center at http://nssdcftp.gsfc.nasa.gov. The PI of the PVO magnetic field data is C.T. Russell, UCLA and the PI of the solar wind data is A. Barnes, NASA Ames Research Center. The OMNI data were obtained from the GSFC/SPDF OMNIWeb interface at http://omniweb.gsfc.nasa.gov. The authors acknowledge the PVO and OMNI data sources and the principal investigators of the data.

References

Barabash, S., A. Fedorov, R. Lundin, and J.-A. Sauvaud (2007a), Martian atmospheric erosion rates, *Science*, *315*, 501–503, doi:10.1126/science.1134358.

Barabash, S., et al. (2007b), The loss of ions from Venus through the plasma wake, *Nature*, *450*, 650–653, doi:10.1038/nature06434.

Brain, D., et al. (2010), *A Comparison of Global Models for the Solar Wind Interaction with Mars, Icarus*, *206*, 139–151, doi:10.1016/j.icarus.2009.06.030.

Cloutier, P. A., R. E. Daniell, and D. M. Butler (1974), Atmospheric ion wakes of Venus and Mars in the solar wind, *Planet. Space Sci.*, *22*, 967–990, doi:10.1016/0032-0633(74)90166-4.

Coates, A. J. (1997), Ionospheres and magnetospheres of comets, *Adv. Space Res.*, *20*, 255–266, doi:10.1016/S0273-1177(97)00543-7.

Coates, A. J. (2004), Ion pickup at comets, *Adv. Space Res.*, *33*, 1977–1988, doi:10.1016/j.asr.2003.06.029.

Colin, L., and D. M. Hunten (1977), Pioneer venus experiment descriptions, *Space Sci. Rev.*, *20*, 451–525, doi:10.1007/BF02186463.

Cravens, T. E., A. Hoppe, S. A. Ledvina, and S. McKenna-Lawlor (2002), Pickup ions near Mars associated with escaping oxygen atoms, *J. Geophys. Res.*, *107*(A8), 1170, doi:10.1029/2001JA000125.

Edberg, N. J. T., et al. (2011), Atmospheric erosion of Venus during stormy space weather, *J. Geophys. Res.*, *116*, A09308, doi:10.1029/2011JA016749.

Fang, X., M. W. Liemohn, A. F. Nagy, Y. Ma, D. L. De Zeeuw, J. U. Kozyra, and T. H. Zurbuchen (2008), Pickup oxygen ion velocity space and spatial distribution around Mars, *J. Geophys. Res.*, *113*, A02210, doi:10.1029/2007JA012736.

Fedorov, A., et al. (2008), Comparative analysis of Venus and Mars magnetotails, *Planet. Space Sci.*, *56*, 812–817, doi:10.1016/j.pss.2007.12.012.

Fedorov, A., S. Barabash, J.-A. Sauvaud, Y. Futaana, T. L. Zhang, R. Lundin, and C. Ferrier (2011), Measurements of the ion escape rates from Venus for solar minimum, *J. Geophys. Res.*, *116*, A07220, doi:10.1029/2011JA016427.

Futaana, Y., et al. (2008), Mars Express and Venus Express multi-point observations of geoeffective solar flare events in December 2006, *Planet. Space Sci.*, *56*, 873–880, doi:10.1016/j.pss.2007.10.014.

Hartle, R. E., M. Sarantos, and E. C. Sittler Jr. (2011), Pickup ion distributions from three-dimensional neutral exospheres, *J. Geophys. Res.*, *116*, A10101, doi:10.1029/2011JA016859.

Jarvinen, R., E. Kallio, I. Sillanpää, and P. Janhunen (2008), Hybrid modelling the Pioneer Venus Orbiter magnetic field observations, *Adv. Space Res.*, *41*, 1361–1374, doi:10.1016/j.asr.2007.10.003.

Jarvinen, R., E. Kallio, P. Janhunen, S. Barabash, T. L. Zhang, V. Pohjola, and I. Sillanpää (2009), Oxygen ion escape from Venus in a global hybrid simulation: Role of the ionospheric O^+ ions, *Ann. Geophys.*, *27*, 4333–4348.

Jarvinen, R., E. Kallio, S. Dyadechkin, P. Janhunen, and I. Sillanpää (2010), Widely different characteristics of oxygen and hydrogen ion escape from Venus, *Geophys. Res. Lett.*, *37*, L16201, doi:10.1029/2010GL044062.

Jarvinen, R., E. Kallio, and S. Dyadechkin (2013), Hemispheric asymmetries of the Venus plasma environment, *J. Geophys. Res. Space Physics*, *118*, 4551–4563, doi:10.1002/jgra.50387.

Johansson, E. P. G., J. Mueller, and U. Motschmann (2011), Interplanetary magnetic field orientation and the magnetospheres of close-in exoplanets, *Astron. Astrophys.*, *525*, A117, doi:10.1051/0004-6361/201014802.

Kallio, E., and R. Jarvinen (2012), Kinetic effects on ion escape at Mars and Venus: Hybrid modeling studies, *Earth Planets Space*, *64*, 157–163, doi:10.5047/eps.2011.08.014.

King, J. H., and N. E. Papitashvili (2005), Solar wind spatial scales in and comparisons of hourly Wind and ACE plasma and magnetic field data, *J. Geophys. Res.*, *110*, A02104, doi:10.1029/2004JA010649.

Lammer, H., J. F. Kasting, E. Chassefière, R. E. Johnson, Y. N. Kulikov, and F. Tian (2008), Atmospheric escape and evolution of terrestrial planets and satellites, *Space Sci. Rev.*, *139*, 399–436, doi:10.1007/s11214-008-9413-5.

Ledvina, S. A., Y. Ma, and E. Kallio (2008), Modeling and simulating flowing plasmas and related phenomena, *Space Sci. Rev.*, *139*, 143–189, doi:10.1007/s11214-008-9384-6.

Liu, K., E. Kallio, R. Jarvinen, H. Lammer, H. I. M. Lichtenegger, Y. N. Kulikov, N. Terada, T. L. Zhang, and P. Janhunen (2009), Hybrid simulations of the O^+ ion escape from Venus: Influence of the solar wind density and the IMF x component, *Adv. Space Res.*, *43*, 1436–1441, doi:10.1016/j.asr.2009.01.005.

Luhmann, J. G. (2003), Characteristics of scatter-free behavior of heliospheric pickup ions, *Astrophys. J.*, *592*, 1241–1251, doi:10.1086/375770.

Luhmann, J. G., and K. Schwingenschuh (1990), A model of the energetic ion environment of Mars, *J. Geophys. Res.*, *95*, 939–945, doi:10.1029/JA095iA02p00939.

Luhmann, J. G., C. T. Russell, J. L. Phillips, and A. Barnes (1987), On the role of the quasi-parallel bow shock in ion pickup - A lesson from Venus?, *J. Geophys. Res.*, *92*, 2544–2550, doi:10.1029/JA092iA03p02544.

Luhmann, J. G., T. Zhang, S. M. Petrinec, C. T. Russell, P. Gazis, and A. Barnes (1993), Solar cycle 21 effects on the interplanetary magnetic field and related parameters at 0.7 and 1.0 AU, *J. Geophys. Res.*, *98*, 5559–5572, doi:10.1029/92JA02235.

Luhmann, J. G., S. A. Ledvina, J. G. Lyon, and C. T. Russell (2006), Venus O^+ pickup ions: Collected PVO results and expectations for Venus Express, *Planet. Space Sci.*, *54*, 1457–1471, doi:10.1016/j.pss.2005.10.009.

Luhmann, J. G., A. Fedorov, S. Barabash, E. Carlsson, Y. Futaana, T. L. Zhang, C. T. Russell, J. G. Lyon, S. A. Ledvina, and D. A. Brain (2008), Venus Express observations of atmospheric oxygen escape during the passage of several coronal mass ejections, *J. Geophys. Res.*, *113*, E00B04, doi:10.1029/2008JE003092.

Lundin, R. (2011), Ion acceleration and outflow from Mars and Venus: An overview, *Space Sci. Rev.*, *162*, 309–334, doi:10.1007/s11214-011-9811-y.

McEnulty, T. R., J. G. Luhmann, I. de Pater, D. A. Brain, A. Fedorov, T. L. Zhang, and E. Dubinin (2010), Interplanetary coronal mass ejection influence on high energy pick-up ions at Venus, *Planet. Space Sci.*, *58*, 1784–1791, doi:10.1016/j.pss.2010.07.019.

Nilsson, H., G. Stenberg, Y. Futaana, M. Holmström, S. Barabash, R. Lundin, N. J. T. Edberg, and A. Fedorov (2012), Ion distributions in the vicinity of Mars: Signatures of heating and acceleration processes, *Earth Planets Space*, *64*, 135–148, doi:10.5047/eps.2011.04.011.

Nordström, T., G. Stenberg, H. Nilsson, S. Barabash, and T. L. Zhang (2013), Venus ion outflow estimates at solar minimum: Influence of reference frames and disturbed solar wind conditions, *J. Geophys. Res. Space Physics*, *118*, 3592–3601, doi:10.1002/jgra.50305.

Parker, E. N. (1963), *Interplanetary Dynamical Processes.*, 272 pp., John Wiley, New York.

Phillips, J. L., J. G. Luhmann, C. T. Russell, and K. R. Moore (1987), Finite Larmor radius effect on ion pickup at Venus, *J. Geophys. Res.*, *92*, 9920–9930, doi:10.1029/JA092iA09p09920.

Slavin, J. A., and R. E. Holzer (1981), Solar wind flow about the terrestrial planets. I - Modeling bow shock position and shape, *J. Geophys. Res.*, *86*, 11,401–11,418, doi:10.1029/JA086iA13p11401.

Wei, Y., et al. (2012), Enhanced atmospheric oxygen outflow on Earth and Mars driven by a corotating interaction region, *J. Geophys. Res.*, *117*, A03208, doi:10.1029/2011JA017340.

Zhang, T. L., J. Du, Y. J. Ma, H. Lammer, W. Baumjohann, C. Wang, and C. T. Russell (2009), Disappearing induced magnetosphere at Venus: Implications for close-in exoplanets, *Geophys. Res. Lett.*, *36*, L20203, doi:10.1029/2009GL040515.